Correlation Analysis of Doppler Radar Data and Retrieval of the Horizontal Wind

GLENN R. SMYTHE

Systems and Applied Sciences Corporation, Lexington, MA 02173

DUSAN S. ZRNIC'

National Severe Storms Laboratory/NOAA, Norman, OK 73069

(Manuscript received 23 January 1982, in final form 28 October 1982)

ABSTRACT

A technique for tracking patterns of radial velocity and reflectivity data obtained with a single-Doppler radar is described. Application of the technique to two different scans of the same spatial region may lead to the extraction of a field of "wind" vectors with both radial and azimuthal components. This is accomplished by displacing, in range and azimuth, small volumes or "boxes" of data from the earlier scan and then correlating them with boxes of equal dimensions from the later scan. The displacements at which correlation coefficients maximize are assumed to be due to the advection of patterns existing at scales up to the "box" dimensions.

Correlation coefficients of radial velocities are shown, for the clear air cases analyzed, to be higher than those of reflectivity [dB(Z)]. "Winds" retrieved by correlating velocities and reflectivities independently are compared with each other and with winds synthesized from dual-Doppler radar data. Winds from radial velocity correlations agree better with the dual-Doppler winds than do winds from reflectivity correlations. Convective rolls spaced ~5 km apart are revealed in the planetary boundary layer.

1. Introduction

Since their advent, Doppler radars have been important tools for observing the kinematic structure of the lower troposphere. Systems of two and three Doppler radars have been utilized to map horizontal and vertical wind fields with reasonable accuracy. In this paper we propose a one-radar technique based on correlation and pattern recognition, which in some instances may yield two-dimensional wind flow.

Hilst and Russo (1960) were the first to employ correlation analysis to forecast storm cell displacement. Kessler and Russo (1963) continued their study and computed length scales and lifetimes of recognizable patterns. They found that reliability of storm displacement was dependent upon lifetimes of the patterns. Crane (1979) and Bjerkaas and Forsyth (1980) searched for well-defined cells and tracked them in later data by matching such attributes as areal extent, mass, relative position and intensity. These methods, however, yield motions of entire storms only.

Conceptually our technique parallels that of Rinehart and Garvey (1978) and Rinehart (1979) which utilized data from a non-Doppler radar. Both techniques correlate regions of data over volumes ~8° by 6 km observed at two different times. We differ from Rinehart in that we take advantage of Doppler radial velocities to estimate radial components of air parcel displacements and then correlate azimuthally until maxima are found. Also, we correlate both radial velocity and reflectivity fields independently.

In general, neither correlation techniques nor any other pattern or cell tracking methods retrieve winds; rather, they produce motions. In the case of reflectivity motions are due either to advection or propagation of that scalar quantity. Since radial velocity is one component of a vector quantity tracking will indicate advection of these components if they are carried by flow on scales larger than the region being correlated; or it will show propagation if these components have "wave-like" behavior. Thus caution must be exercised in interpreting results from such analyses. Of course, in a well-mixed planetary boundary layer (PBL) there will be close correspondence between the mean PBL wind and correlation results at the same height.

2. The technique

Our technique requires data on polar grids from two different scans of the same "horizontal" region. The term "horizontal" is used rather loosely, as the data do not lie on a truly horizontal plane, but do lie on a conical surface with vertex at the radar. The two scans were partitioned into angular sectors, each of which contained several data rays (radials that co-

incide with the radar's beam position). The number of rays thus contained was determined by the choice of arc length of the annular sector that enclosed the entire data analysis region. Then each of the sectors of the first scan was subdivided into boxes (see Fig. 1, in which one box is hatched).

A sector from the second scan was chosen to be wider than a sector from the first scan to allow the shifting of a box, ray by ray (radial by radial), to its azimuthal extremities, as indicated by the longer of the two-headed arrows in Fig. 1. In this paper, the two sectors will be referenced, collectively, as a sector pair. Both scans were partitioned to conserve computer memory.

The mean radial velocity of an air parcel was estimated by averaging all values measured within the bounds of its box. This estimate was used to determine the expected radial displacement of the box, an initial guess as to where correlation for either velocity or reflectivity should be best in range. Limiting the search resulted in reduced computation time. In Fig. 1 the displacement of the hatched box is labeled D.

Correlation coefficients for a box were computed for several azimuthal and range lags; i.e., within ±5 range gates (spaced 150 m apart for a total spread of ±0.75 km) of the expected radial displacement (the shorter of the two-headed arrows in Fig. 1) and within the angular limits of the sector of the second scan. Each coefficient was computed using the familiar equation

$$\rho = \frac{\sum_{i=1}^{N} (a_{1i} - \hat{a}_1)(a_{2i} - \hat{a}_2)}{\left[\sum_{i=1}^{N} (a_{1i} - \hat{a}_1)^2 \sum_{i=1}^{N} (a_{2i} - \hat{a}_2)^2\right]^{1/2}}, \quad (2.1)$$

where

$$\hat{a}_j = \left(\sum_{i=1}^{M} a_{ji}\right) M^{-1},$$

i is the summation index, j identifies the scan (1 or 2), and N is the number of non-missing data points common to both the box and the portion of the second sector with which it was correlated. Caps denote that the quantity is an estimate. (Approximately 15% of data due to weak signals and point targets was removed before processing.) The averages of the a_{1i}'s and a_{2i}'s were computed using all available values corresponding to i, from 1 to M, and result in better estimates than if only the fewer common points were used. The parameter a may be either radial velocity or the reflectivity factor logarithm, 10 log Z [dB(Z)], which we shall call reflectivity. From the array of correlation coefficients a maximum was found and a "velocity" vector formed by dividing the distance between the geometric center of the box at its new position (i.e., where maximum correlation occurred) with the time interval between scans.

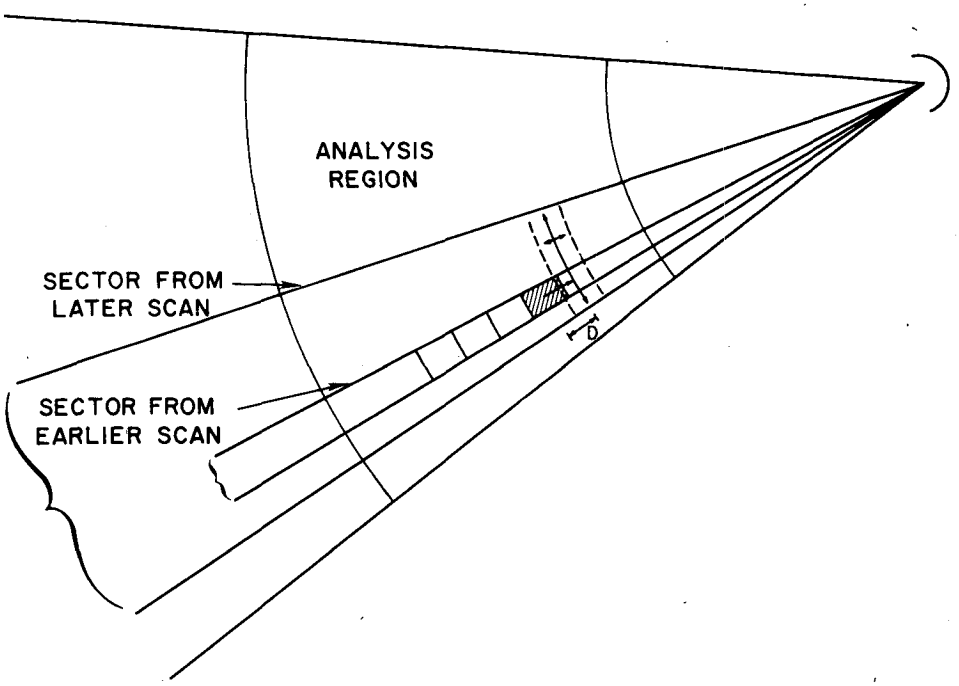

FIG. 1. Depiction of the single-Doppler wind retrieval geometry.

3. Case study of 27 April 1977

a. Wind retrieval

The data used in this study were collected, utilizing the two 10 cm wavelength pulsed Doppler radars of the National Severe Storms Laboratory (NSSL) in Norman, Oklahoma, during the afternoon of 27 April 1977 in an optically clear atmosphere. Dual-radar winds near the surface were from 210° with speeds

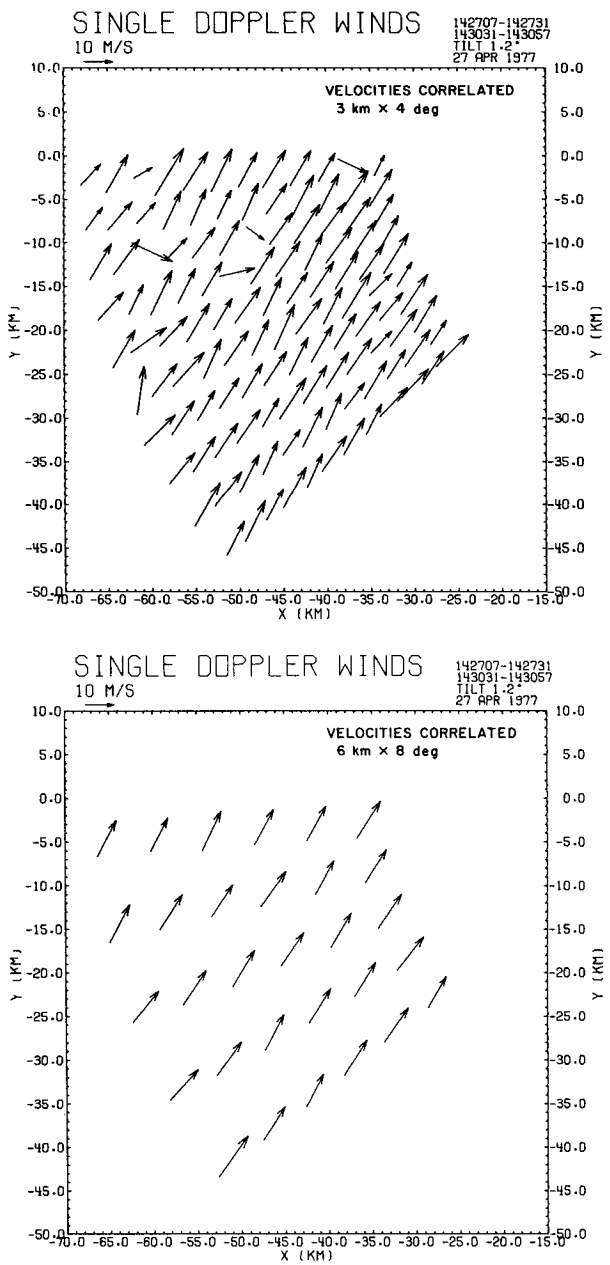

FIG. 2. Single-Doppler winds reconstructed using radial velocities and (a) 3 km × 4° boxes, and (b) 6 km × 8° boxes. Data were collected on 27 April 1977 at 1.2° elevation.

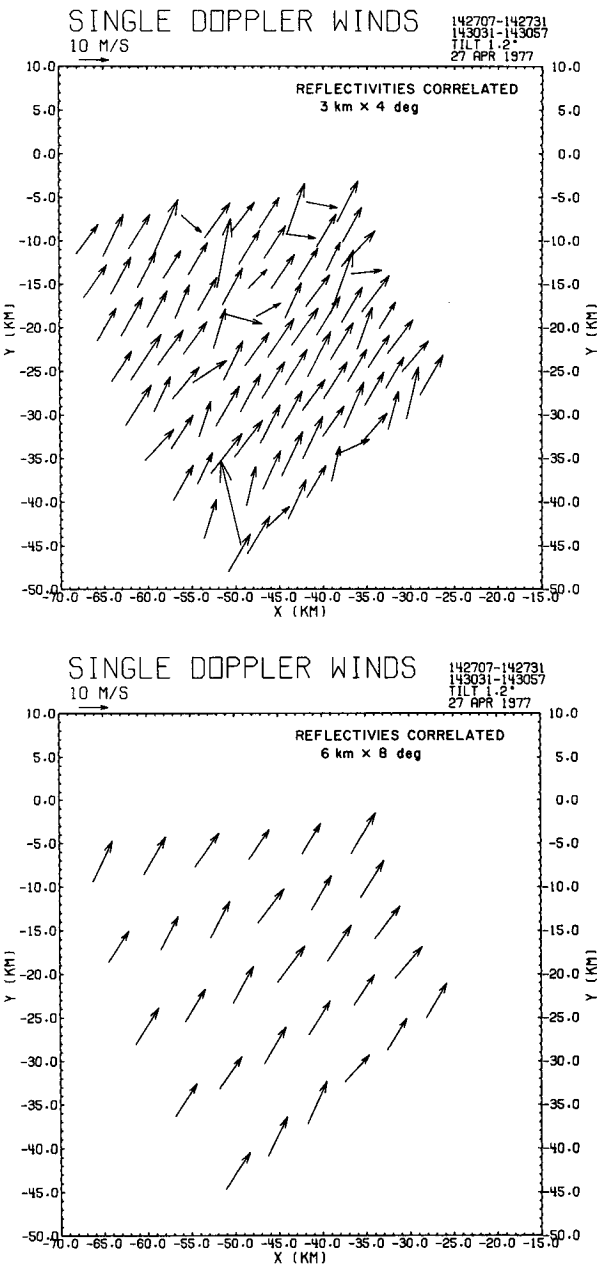

FIG. 3. As in Fig. 2, except that winds were reconstructed using reflectivities [dB(Z)].

of 13–15 m s^{-1} over our 50 km × 50 km analysis region located southwest of Norman. Data from NSSL's Norman radar were used in both single- and dual-radar analyses, while data from the Cimarron radar, located ~40 km northwest of Norman, were used only in the dual-radar synthesis because Cimarron's sensitivity is about 3 dB lower than Norman's.

Doppler velocity and reflectivity fields were analyzed using three box sizes: 3 km × 4°, 6 km × 8°

TABLE 1. Velocity correlations (ρ_{max}).

a. 3 km × 4° boxes

Azimuth (deg)	Range (km) 67.0	64.0	61.0	58.0	55.0	52.0	49.0	46.0	43.0	40.0	37.0	34.0
268.1	0.27	0.27	0.24	0.42	0.46	0.64	0.48	0.65	0.48	0.81	0.44	0.53
263.8	0.28	0.40	0.44	0.41	0.50	0.43	0.48	0.48	0.53	0.63	0.70	0.76
259.5	0.33	0.36	0.29	0.44	0.52	0.50	0.59	0.41	0.51	0.75	0.71	0.45
255.1	0.30	0.59	0.54	0.53	0.56	0.59	0.71	0.67	0.74	0.59	0.60	0.55
250.7	0.29	0.24	0.31	0.40	0.73	0.75	0.59	0.77	0.60	0.52	0.63	0.61
246.8	0.37	0.35	0.59	0.34	0.44	0.47	0.71	0.52	0.59	0.68	0.69	0.47
242.1	0.28	0.34	0.73	0.62	0.69	0.58	0.64	0.73	0.70	0.66	0.59	0.63
237.7	0.25	0.41	0.51	0.52	0.35	0.45	0.60	0.56	0.60	0.50	0.72	0.70
233.3	0.40	0.66	0.48	0.55	0.63	0.63	0.66	0.65	0.73	0.77	0.58	0.63
229.0	0.50	0.60	0.71	0.48	0.66	0.53	0.57	0.59	0.78	0.75	0.72	0.56
Average	0.327	0.422	0.484	0.471	0.554	0.557	0.603	0.603	0.616	0.666	0.638	0.589

b. 6 km × 8° boxes

Azimuth (deg)	Range (km) 65.5	59.5	53.5	47.5	41.5	35.5
265.9	0.25	0.37	0.53	0.63	0.66	0.67
257.1	0.25	0.48	0.51	0.67	0.59	0.72
248.6	0.32	0.48	0.57	0.73	0.69	0.46
239.8	0.38	0.62	0.58	0.66	0.59	0.57
231.2	0.45	0.47	0.48	0.54	0.57	0.65
Average	0.330	0.484	0.534	0.646	0.620	0.614

and 9 km × 12°.[1] The first dimension is the radial length, the second is the arc length in degrees. The radii of the rings of the annulus (see Fig. 1) were 27 and 70 km. These limits were set somewhat arbitrarily; the lower one to reduce the effects of ground clutter and the upper one to ensure that the analysis region remained within the PBL, where signals due to meteorological phenomena are expected to be stronger than background noise. The Norman radar was scanning a sector bounded azimuthally by 225° and 275° at an elevation of 1.2°.

Examples of single-Doppler "wind fields" reconstructed by our technique are shown in Figs. 2 and 3. These fields were extracted by correlating radial velocities and reflectivities, respectively, using 3 km × 4° and 6 km × 8° box sizes. Comparing Figs. 2a with 2b and 3a with 3b, we see that, although the 3 km × 4° box size affords much better resolution, its use leads to a much greater proportion of vectors that are inconsistent with the majority. Spatial variations of wind vectors termed speed variances (σ_T^2) for the 3 km × 4° boxes were larger than 10 $m^2 s^{-2}$ for both reflectivity and velocity correlations, even at the shortest time lag (208 s).

Maximum correlations (ρ_{max}) corresponding to winds in Figs. 2 and 3 are presented in Tables 1 and 2. We see that correlations averaged at each range were highest at ranges closest to the radar when velocities were correlated. Low velocity correlations may be attributed to weak signals from ranges far from the radar. However, reflectivity correlations were constant or decreased slightly up to a certain range, after which they increased in value. This increase is artificial because at larger ranges constant noise power becomes significant. When this power is multiplied by the squares of the corresponding ranges to obtain reflectivity in dB(Z), a fabricated profile of Z versus range results.

Anomalies were more numerous as box size decreased and time lag increased. Distortion due to the polar form of data and deformation of features play important roles as time lag increases (see Appendix). When we compare vector orientations and magnitudes in Figs. 2 and 3 with corresponding values of ρ_{max} in Tables 1 and 2, we see that low maximum correlation coefficients are not always associated with inconsistent arrows, nor are high maximum correlations always indicative of consistent arrows.

Values of average maximum correlation coefficients ($\overline{\rho_{max}}$) and variances in the east-west (x) and north-south (y) components of the single-radar wind

[1] The size of the box limits the smallest recognizable patterns. The number of velocity and reflectivity samples used to compute a correlation coefficient is dependent upon box size, and the number of samples removed by editing. Too few samples yield a poor estimate of the true correlation between a first scan box and its counterpart in the second scan.

TABLE 2. Reflectivity correlations (ρ_{max}).

a. 3 km × 4° boxes

Azimuth (deg)	Range (km) 67.6	64.6	61.6	58.6	55.6	52.6	49.6	46.6	43.6	40.6	37.6
261.6	0.53	0.43	0.60	0.54	0.28	0.41	0.64	0.48	0.28	0.27	0.44
257.4	0.62	0.61	0.57	0.28	0.25	0.33	0.25	0.44	0.29	0.58	0.28
253.1	0.60	0.63	0.66	0.60	0.35	0.54	0.43	0.44	0.41	0.35	0.39
248.8	0.56	0.49	0.68	0.32	0.36	0.26	0.37	0.29	0.42	0.29	0.37
244.7	0.42	0.47	0.27	0.41	0.28	0.46	0.47	0.24	0.45	0.38	0.48
240.3	0.45	0.55	0.52	0.54	0.26	0.50	0.46	0.35	0.41	0.37	0.35
235.9	0.36	0.53	0.28	0.44	0.49	0.53	0.38	0.37	0.53	0.35	0.51
231.6	0.53	0.41	0.32	0.44	0.46	0.51	0.35	0.51	0.48	0.46	0.59
227.3	0.43	0.39	0.49	0.45	0.26	0.39	0.31	0.47	0.36	0.34	0.33
Average	0.500	0.501	0.488	0.447	0.332	0.437	0.407	0.339	0.403	0.377	0.412

b. 6 km × 8° boxes

Azimuth (deg)	Range (km) 65.6	59.5	53.5	47.5	41.5	35.5
263.8	0.40	0.54	0.42	0.44	0.39	0.38
255.1	0.61	0.44	0.29	0.24	0.32	0.30
246.6	0.45	0.40	0.36	0.35	0.28	0.39
238.2	0.45	0.36	0.43	0.38	0.37	0.40
229.4	0.40	0.36	0.35	0.30	0.28	0.34
Average	0.462	0.420	0.370	0.342	0.328	0.362

vector (σ_u^2 and σ_v^2, respectively) and speed variance $\sigma_T^2 = \sigma_u^2 + \sigma_v^2$ for various time lags (Δt) are listed in Table 3. These values result from application of the technique to radial velocity and reflectivity data using the 6 km × 8° box size. Averages of the u and v components ($\bar{u}$ and $\bar{v}$) are given along with standard deviation and magnitude and direction of the mean wind. Speed variance versus time lag is plotted in Fig. 4 and we note that at shorter time lags (<700 s) the variances associated with velocity features are smaller than those associated with reflectivity.

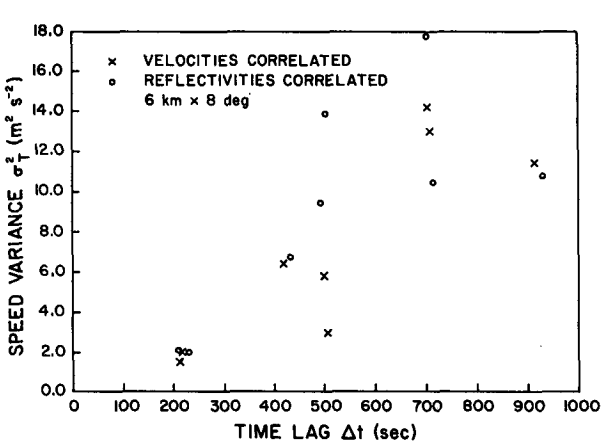

FIG. 4. Speed variance ($\sigma_T^2 = \sigma_u^2 + \sigma_v^2$) versus time lag for velocity and reflectivity correlation analyses using 6 km × 8° boxes.

Each $\overline{\rho_{max}}$ in Table 3 is an average of maximum correlation coefficients computed during one scan pair analysis. Corresponding to each box we have one velocity vector and one ρ_{max}. The time lag (Δt) is the difference between the time of data in the first scan sector and data in the second scan sector. The same Δt is assigned to all sector pairs in the region because there is not more than a 1 s difference between collection times of data within a sector.

In Table 3 the σ_v's are almost consistently higher than the σ_u's. This could be due in part to a larger quantization noise in azimuth, which is aligned with the v direction; i.e., discrete azimuthal increments are larger than the range ones (see Appendix). However, the most likely contributors to the increased σ_v^2 are roll vortices that have axes almost aligned with the radial direction (Section 3c).

b. Comparison with winds obtained from dual-Doppler radar

Wind fields reconstructed using this technique and a dual-Doppler synthesis are compared in Fig. 5. The single-radar fields, derived from velocity correlations using 6 km × 8° boxes, have more widely spaced grid points than the dual-radar fields, so less detail is available in the single radar case. The first scan from the Norman radar was used with a simultaneous scan from Cimarron to construct the dual-Doppler fields. In Fig. 5 (1427 CST case) the single- and dual-radar

TABLE 3. Results from 27 April 1977 case study for 6 km × 8° boxes.

Δt (s)	$\overline{\rho_{max}}$	Number of boxes	σ_u^2 (m^2 s^{-2})	σ_v^2 (m^2 s^{-2})	σ_T^2 (m^2 s^{-2})	$\bar{u} \pm \sigma_u$ (m s^{-1})	$\bar{v} \pm \sigma_v$ (m s^{-1})	$\lvert\bar{v}\rvert$ (m s^{-1})	θ (deg)
				Reflectivity correlated					
209	0.38	30	0.775	1.459	2.233	7.55 ± 0.880	11.87 ± 1.208	14.07	212.5
215	0.44	30	0.873	1.115	1.988	7.46 ± 0.934	11.84 ± 1.056	13.99	212.2
416	0.32	20	2.783	3.966	6.749	7.16 ± 1.668	12.49 ± 1.991	14.40	209.8
494	0.29	20	0.962	8.508	9.469	7.72 ± 0.981	11.24 ± 2.917	13.64	214.5
499	0.30	24	3.065	10.825	13.890	8.34 ± 1.751	11.02 ± 3.290	13.82	217.1
700	0.25	20	4.656	13.077	17.732	8.48 ± 2.158	10.83 ± 3.616	13.75	218.1
707	0.26	20	2.563	7.951	10.513	7.88 ± 1.601	12.76 ± 2.820	15.00	211.7
914	0.25	15	1.764	8.907	10.671	10.18 ± 1.328	9.32 ± 2.984	13.80	227.5
				Velocity correlated					
208	0.54	30	1.088	0.579	1.667	7.51 ± 1.043	11.90 ± 0.761	14.07	212.3
215	0.53	30	0.991	0.982	1.973	7.53 ± 0.995	12.14 ± 0.991	14.29	211.8
416	0.43	30	0.717	5.667	6.384	7.52 ± 0.847	11.62 ± 2.380	13.84	212.9
494	0.43	25	0.657	5.097	5.754	7.59 ± 0.811	11.29 ± 2.258	13.60	213.9
498	0.40	25	0.738	2.253	2.991	7.80 ± 0.859	10.98 ± 1.501	13.47	215.3
702	0.37	20	1.792	12.445	14.237	8.73 ± 1.339	11.17 ± 3.528	14.18	218.0
707	0.36	20	2.129	10.815	12.944	8.71 ± 1.459	11.05 ± 3.229	14.07	218.2
913	0.33	10	3.447	8.251	11.698	9.42 ± 1.857	10.98 ± 2.872	14.47	220.6

winds exhibit turning to a more southerly flow as the air moved from south to north. For the 1430 CST case (not shown) this same turning was evident. Thus the single-radar correlation technique is capable of mapping small changes in wind direction.

Although dual-Doppler wind analysis and single-Doppler analysis are two independent error prone techniques, it is logical to assume that winds obtained from two radars would be closer to the truth. For instance, propagation effects could render the correlation technique useless but would not bias wind fields obtained from two radars. Therefore, for the purpose of this study we define speed "errors" between wind vectors obtained by single and dual radars as

$$\left.\begin{aligned} \epsilon_u^2 &= \sum (u_{dd} - u_{sd})^2/N \\ \epsilon_v^2 &= \sum (v_{dd} - v_{sd})^2/N \\ \epsilon_T^2 &= \epsilon_u^2 + \epsilon_v^2 \end{aligned}\right\}, \qquad (3.1)$$

where ϵ_u and ϵ_v are "errors" in the east-west and north-south components of the "horizontal" wind, respectively, and ϵ_T is the speed "error" in the single-radar wind field.

Speed errors for the three box sizes are compared in Fig. 6. Dual-radar vectors centered closest to the single-radar vectors were used in these comparisons. Most obvious are the larger errors associated with the 3 km × 4° box size (also, compare Figs. 2a and 2b). These imply, along with the large variances of 3 km × 4° resolved wind fields, that, with increasing resolution, the quality of the flow field degrades. We suspect that this is because many more turbulent eddies of length scales < 3 km have similar characteristics than do features of scales on the order of 6–9 km which contain several of the smaller eddies. The box size 6 km × 8° is large enough to include several eddies corresponding to the 4–5 km periodicities which were deduced from oscillations in the correlation function (see Sections 3c and 4). Therefore the 6 km × 8° box size offers the best compromise between variance and resolution since the rms errors

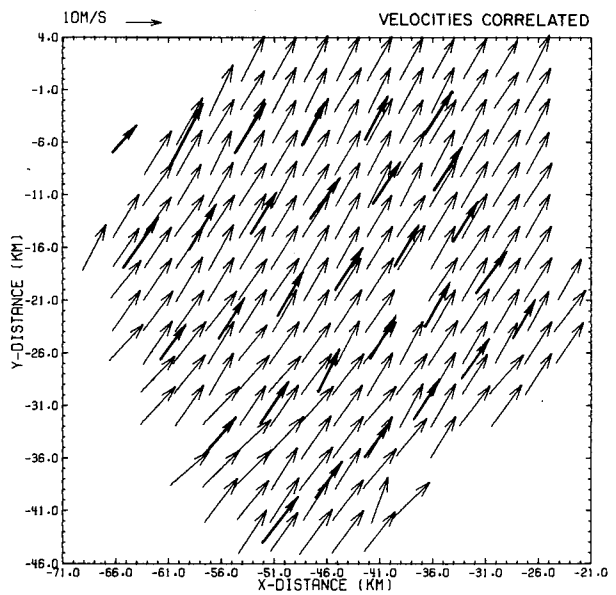

FIG. 5. Comparison of single-radar winds (bold arrows) with dual-radar winds at 1427 CST. Winds were obtained using 6 km × 8° boxes and by correlating data from scan time 1427 CST with 1431 CST.

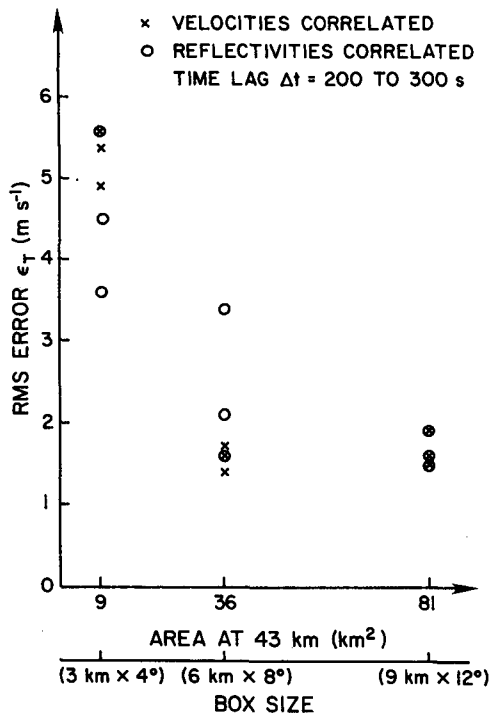

FIG. 6. Root mean square errors between single-radar and dual-radar winds. $\epsilon_T = (\epsilon_u^2 + \epsilon_v^2)^{1/2}$ for the three box sizes.

and variances (σ_T^2 larger than 10 m^2 s^{-2}, see Section 3a) are very high at short time lags (<300 s) for 3 km × 4° boxes, while 9 km × 12° boxes produce coarser resolution. Thus we shall continue looking at time lags only for 6 km × 8° boxes.

Fig. 7 shows errors for lags 210 s and longer when velocities and reflectivities were correlated. There is a trend toward increasing error with increasing time lag. Errors in speed from radial velocity correlation exceeded those obtained from reflectivity correlation for only two time lags, 416 and 706 s. This, along with the higher correlations ($\overline{\rho_{max}}$) of velocity from Table 3, suggests that, at least for these data, it is more advantageous to correlate Doppler velocities than to correlate reflectivities. In all cases examined the error components in the v direction were consistently larger (sometimes by a factor of 2) than the ones in the u direction, which is in harmony with the respective variances. We thus conclude that the natural variability of wind fields is responsible for the differences between single- and dual-Doppler derived results at longer time lags. A more detailed error analysis is presented in the Appendix.

c. *Convective rolls and their effects on wind retrieval*

Over portions of the radial velocity field the correlation exhibited oscillatory behavior as a function of azimuthal lag. Fig. 8 shows correlation contours for an array lagged in time (208 s), azimuth ($\Delta\theta$) and range (Δr). The coherence in range of the velocity correlation function is very apparent. This structure suggests that the contours are ellipses, nearly aligned with the data rays. Elongation is exaggerated due to different scaling factors of range and azimuth axes used for the display. In Fig. 9 we see that it is possible to find a false correlation maximum due to the highly coherent quasi-periodic structure; see the caption for details. Equi-spaced peaks (and valleys) of correlation suggest the existence of convectively driven circulations (Le Mone, 1973). These two-dimensional secondary circulations in the presence of substantial vertical wind shear were independently detected by aircraft (Reinking *et al.*, 1981) and Doppler radars (Doviak and Berger, 1980; Rabin *et al.*, 1982). The spurious maxima are most pronounced when the smallest arrays (3 km × 4°) are analyzed. For the largest arrays (9 km × 12°) this problem does not exist. The presence of this structure accounts for some false vectors that appear in Fig. 2a. Erroneous vectors may also result from the difficulty in detecting maximum correlation near a relatively flat peak.

Doviak and Berger (1980) reported on the manifestation of horizontal roll vortices in these clear air data. They observed secondary peaks in velocity spatial spectra at wavelengths near 4 km. In Fig. 10 correlation coefficients are plotted versus azimuthal lag. Each curve represents arrays lagged at Δt = 208 s and

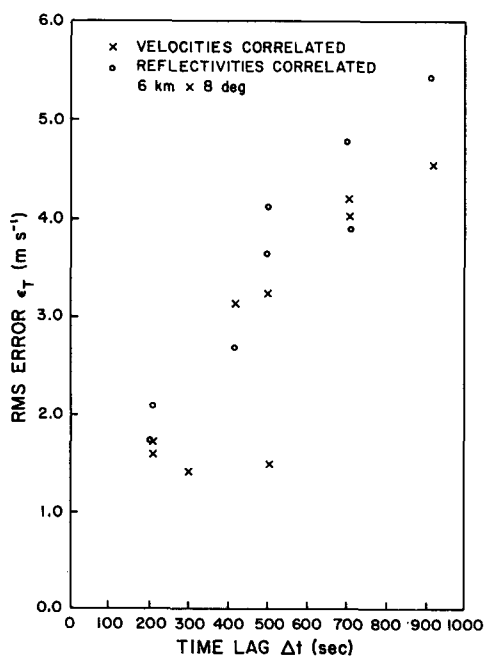

FIG. 7. Root-mean-square error versus time lag for velocity and reflectivity correlation analysis using 6 km × 8° boxes.

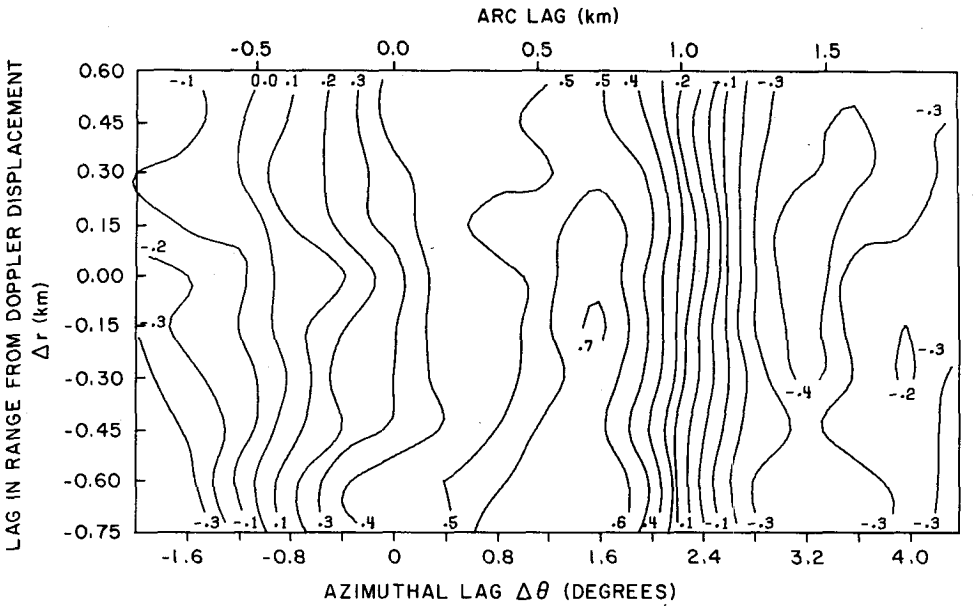

FIG. 8. Azimuth versus range formatted correlation coefficient contours, showing a maximum of 0.70 near +1.6 azimuthal lag and −0.15 km range lag. This corresponds very well to where the best correlation should occur. Zero range lag corresponds to the radial displacement computed from Doppler velocities, and zero azimuthal lag corresponds to the box's initial position. Time between scans was ~208 s. Displacement (Δr = 0) is approximately 26 km from radar and box size is 6 km × 8°.

different ranges from the radar and centered at the range where ρ_{max} was found. Also shown are lengths of 4–5 km, very close to the dominant spacings between rolls observed by Doviak and Berger (1980). We notice that the values of the correlation coefficients are much lower at 67 km than at 34 km. This

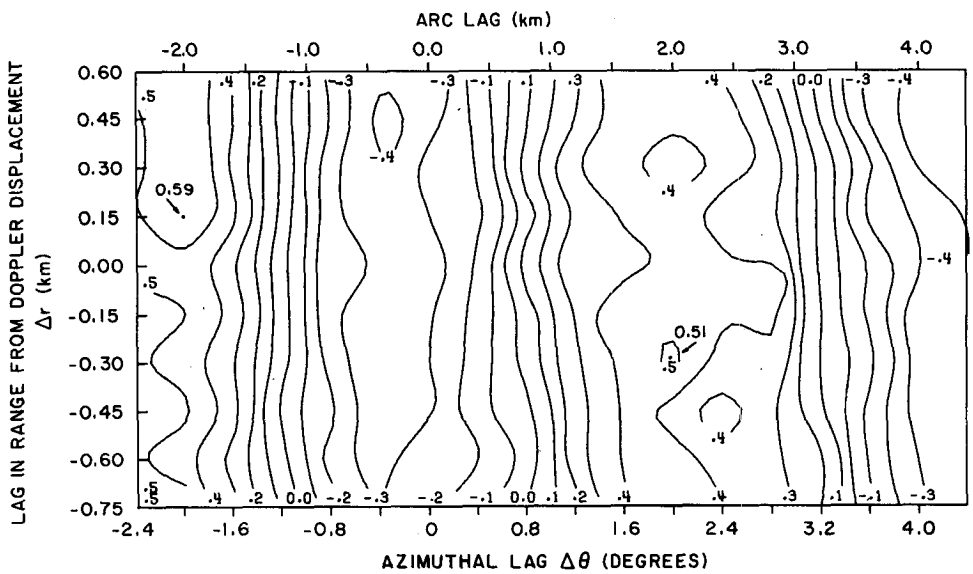

FIG. 9. As in Fig. 8, but with a deceptive, spurious maximum of 0.59 at −2° azimuthal lag and 0.15 km range lag. The secondary maximum of 0.51 at 2° and −0.3 km is only slightly smaller than the first and corresponds to where the feature has actually advected. The erroneous maximum may have been produced by noise since the signal-to-noise ratio at this range (52 km) is 6 dB less than in the case of Fig. 8.

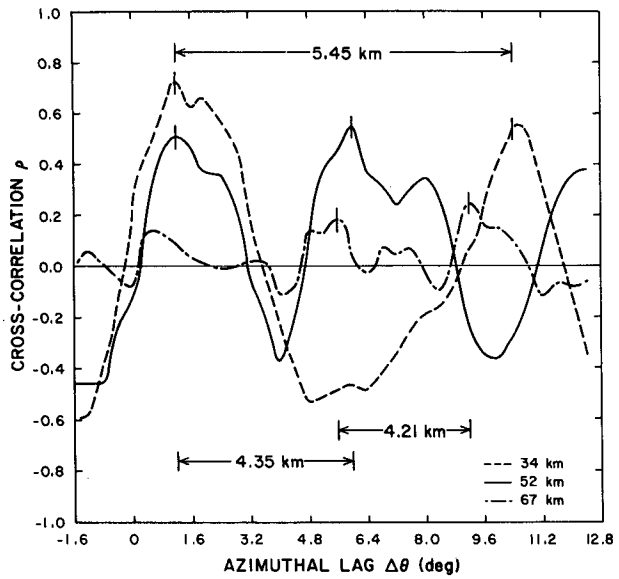

FIG. 10. Cross-correlations of velocities at 1430 and 1435 CST showing patterns that strongly suggest horizontal rolls. Periodic structures of comparable wavelengths are evident for boxes at different ranges. The box size is 6 km × 8° and three ranges from radar to center of boxes are indicated. Boxes were lagged between azimuths 225° and 240°.

is most likely due to noise overriding the strength of the meteorological signal at distant ranges.

Reflectivity streets (Kuettner, 1959), shown in a PPI display taken from 27 April 1977 (Fig. 11), are at 10–20° clockwise from 210°, the direction of the dual-Doppler mean wind. When a box is lagged azimuthally, its path is almost perpendicular to the streets. Because these streets are nearly periodic, so also will be the correlation function in azimuthal lag space at constant time lag.

4. Comparisons of correlation functions for velocity and reflectivity fields

Spatial and temporal behavior of correlation functions relates directly to the accuracy with which reflectivity or velocity patterns can be tracked. For instance, in the Appendix it is shown that standard errors are inversely proportional to the sharpness of the peak of the cross-correlation function. From the temporal decay of these functions one can find an upper limit for the time lag beyond which tracking by correlation may not be reliable. Of course, for studies of atmospheric turbulence knowledge of correlations is essential.

Doppler radar provides a unique opportunity to measure both the spatial and temporal behavior of the correlation functions. This is so because data throughout the PBL can be obtained in a short time period (less than 3 min for this study), so that for most practical purposes a frozen three-dimensional picture of turbulence quantities is obtained.

We shall now examine the spatial and temporal behavior of the correlation functions of velocity and reflectivity. Spatial lag correlation coefficients were computed by averaging coefficients produced by lagging, in ranges, boxes (9 km × 12°) of reflectivity or

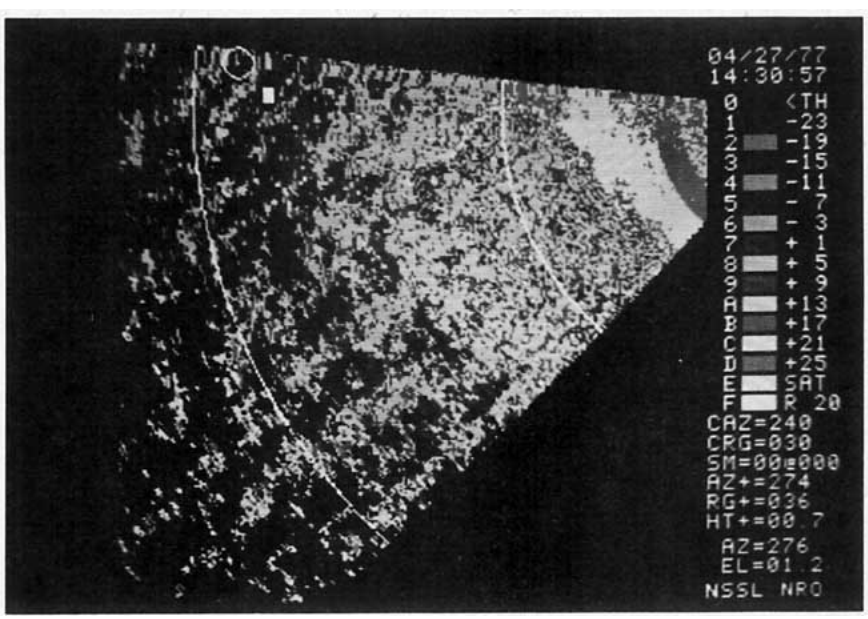

FIG. 11. PPI sector display showing reflectivity streets at 1430 CST 27 April 1977.

radial velocity data. The tolerance of ±5 range gates was increased to ±10 gates (i.e., ±1.5 km) to obtain correlation estimates over an expanded range. Correlation coefficients were averaged azimuthally; several azimuthally adjacent boxes contributed to calculating the average coefficient. Coefficients for study of the space-time correlation function were found in like manner, whereas temporal correlations were found by averaging correlation coefficient maxima over the entire analysis region.

Radial lags were chosen for this part of the study because fluctuations in correlation in the azimuthal direction are heavily dominated by the presence of horizontal rolls. For the analyzed region there were no discernible periodicities along the radial component.

a. Autocorrelation in the spatial domain

We look first at two typical examples of the spatial autocorrelation function (Fig. 12). The solid curve represents the velocity correlation function, the dashed curve the reflectivity function, and both result from using 9 km × 12° boxes. Autocorrelation coefficient ρ is plotted against spatial lag Δs in both examples. We see that, in the spatial domain, reflectivity decorrelates much more rapidly than does velocity. This was true for all cases.

A possible explanation for the difference in scale sizes can be found in the generating mechanisms of velocity and reflectivity fluctuations. It seems that reflectivity fluctuations along the rolls are not coupled to velocity fluctuations resolvable by the radar. The reflectivity fluctuations are primarily due to small plumes and convective bubbles emanating from the earth's surface. These are rising slowly without significantly disturbing the velocity structure which is driven by larger scales and is nearly independent of local conditions.

Because of this difference in scale sizes we expect velocity perturbations to have longer lifetimes and thus be more suitable for "wind" retrieval via correlation techniques. This indeed is true as will be seen in the following section.

b. Correlation in the temporal domain

We now examine the temporal behavior of the correlation functions corresponding to velocity and reflectivity for 9 km × 12° and 6 km × 8° boxes. Fig. 13 depicts these cross correlations as function of time. Each data point represents the mean correlation coefficient computed by averaging maximum correlation coefficients in scan pair cross-correlation analyses, as explained in the beginning of Section 4.

Velocity correlations in Fig. 13 are fitted by least squares using $\rho_0[1-(t/t_0)^{2/3}]$ which is a form proposed by Chandrasekhar (1955). Since there is no known "law" for reflectivity correlation in time, no curves are drawn through the reflectivity data in Fig. 13. Characteristic lifetimes (t_0) on the order of 35–40 min were found. For the 9 km × 12° box size ρ_0 equalled 0.69, while for the 6 km × 8° size ρ_0 equalled 0.66. We find that signal-to-noise ratios $[\rho_0/(1-\rho_0)]$ are 2.23 and 1.94, respectively, which confirms that the larger 9 km × 12° size is a better choice for estimating horizontal winds than the 6 km × 8° size.

Note (Fig. 13) the 20% higher value of the correlation coefficients for velocity than for reflectivity. Reflectivity correlation in Rinehart's analyses (Rinehart, 1979, p. 107) had considerably higher values (as much as 100% higher) than our reflectivity correlations. His high correlations might be attributable to stronger signal-to-noise ratios obtainable from

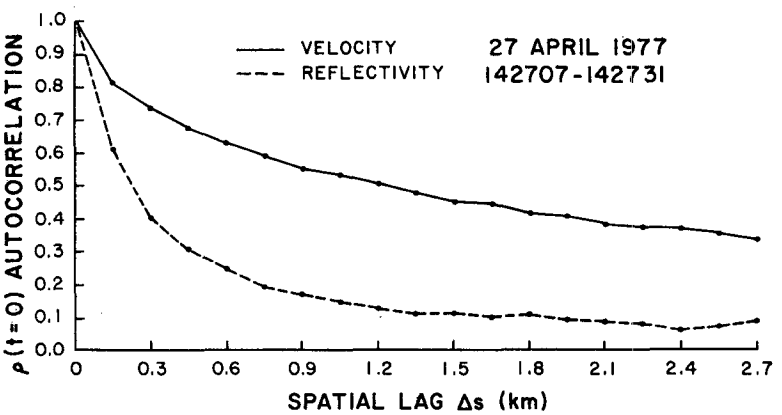

FIG. 12. Comparison of velocity autocorrelation with reflectivity and autocorrelation at 1427 CST. The box size is 9 km × 12° and the values are averages over the analysis region.

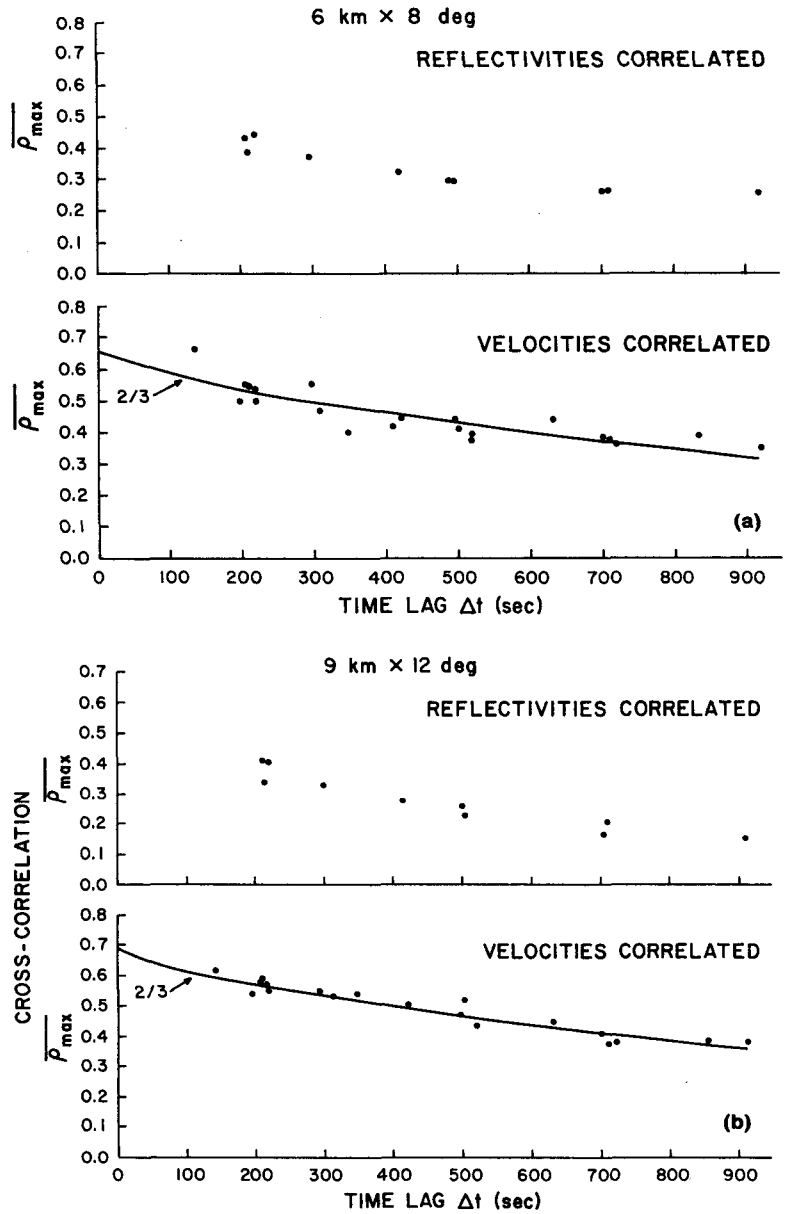

FIG. 13. Comparison of velocity and reflectivity temporal autocorrelations using (a) 6 km × 8° boxes and (b) 9 km × 12° boxes.

storms. It would be most interesting to compare velocity and reflectivity correlation maxima in the case of large signal-to-noise ratios from within strong thunderstorms.

c. *Space-time correlation*

Finally, we shall examine correlation functions resulting from lagging boxes in both space and time. Shown in Figs. 14 and 15 are curves and data points resulting from correlating one scan with the next one (210 s later) at lags of 150 m. In Fig. 14 reflectivities were correlated and in Fig. 15 velocities were correlated, both over the same area. In these cases, zero spatial lag corresponds to the radial displacement obtained by multiplying the 210 s time lag with the average Doppler velocity of a box.

Very apparent is the difference in peak correlations of velocity and reflectivity. For the cases shown, peak correlation coefficients for velocity were as much as 50% higher than the peak coefficients for reflectivity. Also, in all cases not shown, velocity correlation peaks

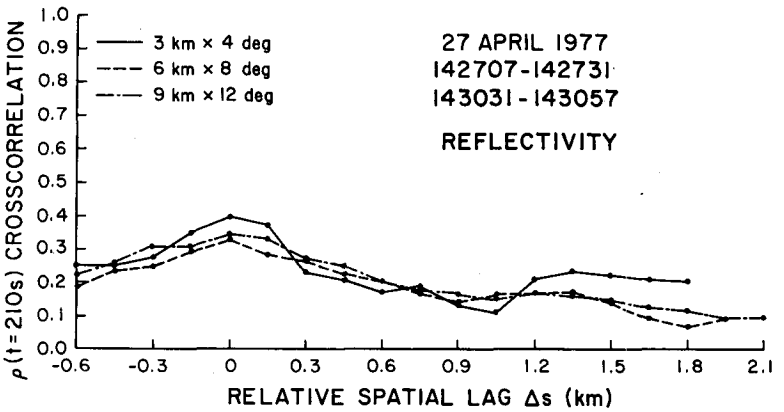

FIG. 14. Reflectivity cross-correlations in space and time for three box sizes. Relative spatial lag is in range and with respect to the Doppler displacement.

were higher than reflectivity correlation peaks. Noticeable is the chaotic nature of the curves corresponding to the smallest box size.

5. Summary and conclusions

A technique for retrieving nearly horizontal "winds" by correlation from single-Doppler radar data has been presented. Azimuthal as well as radial components of the vector wind field have been reconstructed from reflectivity and radial velocity data collected in optically clear air. Doppler radial velocities were incorporated into the analysis as first-guess approximations of the radial components. Very good agreement with dual-Doppler winds has been achieved, particularly when radial velocities were correlated. Overall, radial velocities had higher correlations than reflectivities.

Reflectivity was observed to decorrelate, in space, much more rapidly than radial velocity. The ratio of decorrelation distances of reflectivity and velocity is approximately 0.18. If scale sizes are defined as the length at which the correlation coefficient first drops to 0.5, then velocity scales were about 2 km versus 300 m for reflectivity. Corresponding lifetimes were about 500 s for velocities and less than 200 s for reflectivities.

Periodicity in the correlation function was found and was due to horizontal roll vortices which were manifested as "streets" in the reflectivity field. This motion was, at times, the cause of spurious correlation maxima and a few bad wind vectors.

The correlation technique cannot distinguish between the motion of bulk fluid and the propagation of a wave-like disturbance that may be different from the mean flow in which it is imbedded. Therefore an observer must be careful in interpreting wind vectors; he may be helped by the fact that the Doppler radar provides three spectral components for correlation. Moreover, he has available the true radial component (Doppler) of air motion and if it differs consistently from the one indicated by correlation of either spec-

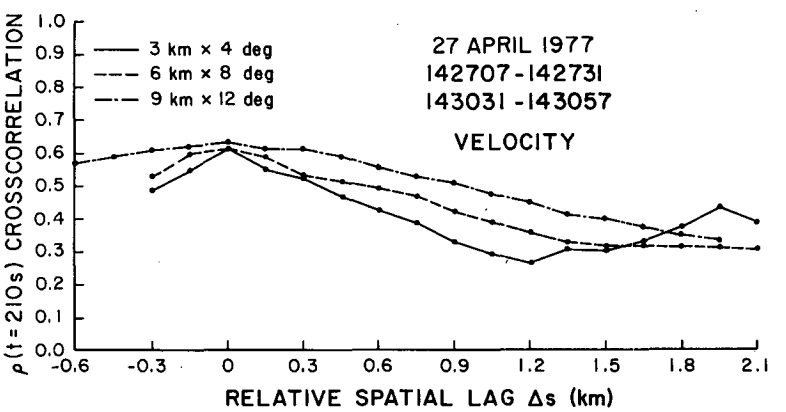

FIG. 15. As in Fig. 14, except velocity was cross-correlated. Note the higher peaks in the velocity correlations.

tral moment it could be due to a wavelike propagation.

Acknowledgments. The authors are indebted to members of NSSL for providing the fine data set on which this study was based, and in particular to Dr. R. J. Doviak, who suggested the problem and made valuable contributions toward its solution. Messrs. M. Weible, L. Fortner and W. Bumgarner were instrumental in helping us overcome programming difficulties. We thank Dr. A. R. Bohne of the Air Force Geophysics Laboratory and Dr. F. I. Harris and Mr. R. J. Donaldson of Systems and Applied Sciences Corporation for their comments on an earlier manuscript. Dr. A. M. Gerlach's editorial review is much appreciated. Also, we appreciate the constructive criticisms of an anonymous reviewer which helped in the refinement of this paper. Much of the computer work was accomplished while G. R. S. was associated with NSSL and the Cooperative Institute for Mesoscale Meteorological Studies. Graphical services reflect the work of J. Kimpel and the manuscript was typed by D. M. Connor.

APPENDIX

Error Analysis

In general, velocity correlation coefficients for boxes far from the radar are smaller than those for boxes near the radar. This can be attributed to lower signal power at greater distances from the radar and also to quantization noise which is enhanced as arc separation between data points increases with range.

1. Inherent errors

Consider the correlation coefficient as given by (2.1) and assume that the expected value

$$E(a_1^2) = E(a_2^2) = A^2. \tag{A1}$$

Furthermore, suppose that uncorrelated noise contaminates the velocity or reflectivity fields. Then the expected value of (2.1) will be approximated by the ratio of expected values of the numerator and denominator:

$$E(\rho) \approx \frac{A^2(\rho_t - \beta)}{A^2(1 - \gamma) + e^2}, \tag{A2}$$

where ρ_t is the temporal correlation,

$$\rho_t = E(a_{1i}a_{2i})A^{-2}, \tag{A3}$$

$$\beta = E[\sum_{i,j}^{M} a_{1i}a_{2j}]M^{-2}A^{-2}, \tag{A4}$$

$$\gamma = E[\sum_{i,j}^{M} a_{1i}a_{1j}]M^{-2}A^{-2}, \tag{A5}$$

e^2 is the noise power ($m^2\ s^{-2}$) and M the number of points used. Other assumptions leading to (A2) are that fourth-order moments of a's can be expressed as sums of the products of second-order moments, as when the variables are Gaussian.

Of the three terms (A3), (A4) and (A5) the first and third can be readily estimated. For instance, ρ_t is the maximized correlation coefficient between data from the first and second scans; γ is the autocorrelation coefficient estimate for the data of the first scan and is assumed to be the same for the second scan. This estimate has a two-dimensional window applied to it via the finite summation in (A5). For a large number of data points γ can be calculated if the correlating region (box) is circular with a radius c, i.e.,

$$\gamma = \int_0^{2c} n(r)[1 - (r/r_0)^{2/3}]dr, \tag{A6}$$

where $n(r)$ is the number density of data points spaced a distance r apart in the circular region and the term in brackets is the correlation function assumed to follow the 2/3 law. It can be shown that $n(r)$ is well approximated by

$$n(r) = \begin{cases} \frac{12}{5} r\left(c^2 - \frac{cr}{2} - \frac{r^2}{6}\right), & 0 < r < c \\ \frac{12}{5} r\left(\frac{2}{3}\frac{c^3}{r} + \frac{r^2}{6} - \frac{cr}{2}\right), & c < r < 2c. \end{cases} \tag{A7}$$

Because we do not know the form of the space-time correlation function we choose to approximate β with the product of temporal correlation ρ_t and the estimate of spatial autocorrelation γ, i.e.,

$$\beta \approx \rho_t\gamma. \tag{A8}$$

We replace the problem of estimating position from the maximum of the cross correlation with the centroid of the cross-correlation. This enables us to use existing results for estimates of the center frequency of Gaussian spectra (Berger and Groginsky, 1973). Thus the variance in the azimuthal position x becomes

$$\text{var}(x) = \frac{(L\Delta s)^2}{L} \times \left\{\frac{\sigma(t)}{L\Delta s 4\sqrt{\pi}} + 2\left[\frac{\sigma(t)}{L\Delta s}\right]^2 \frac{N}{S} + \frac{1}{12}\frac{N^2}{S^2}\right\}, \tag{A9}$$

where L is the number of lags over which one is searching both sides of the correlation maximum, Δs is the data spacing in azimuth, and $\sigma(t)$ is the width of the cross-correlation which may be a function of temporal separation between scans. N is the total noise and S total signal power (i.e., the sum of signal and noise over L points).

These powers are non-dimensional because they

are values of the correlation coefficient squared. The noise power per correlation estimates can be calculated by considering noise alone with a result that

$$N = LM^{-1} \tag{A10}$$

and the signal power is

$$S = \frac{A^2(1-\gamma)}{A^2(1-\gamma)+e^2}\rho_t \sum_{n=-L/2}^{L/2} \exp\left[-\frac{n^2\Delta s^2}{2\sigma^2(t)}\right]$$

$$\approx \frac{A^2(1-\gamma)\rho_t\sigma(t)\sqrt{2\pi}}{[A^2(1-\gamma)+e^2]\Delta s}. \tag{A11}$$

It is intuitively satisfying to observe that the signal power depends directly on the temporal correlations. Also, constant fields without structure ($\gamma = 1$) produce zero correlation coefficients. The inverse dependence on Δs is to be expected since when other variables remain the same there are fewer points for calculating the cross-correlations when Δs is larger.

We shall insert some typical values in (A10) and (A11) which will illustrate order-of-magnitude effects. For the box size 9 km $\times$ 12° we take c to be the average of range and azimuth extent, which at 52 km is 5 km. Because the average r_0 is 14 km we find γ from (A6) to be 0.42. Furthermore, from Fig. 13 we find $A^2/e^2 \simeq 2$ and from Fig. 15 we find $\rho_t = 0.6$ and $\sigma(t) \simeq 0.85$ km at $t = 210$ s. The azimuthal spacing of 0.5° corresponds to a distance $\Delta s = 450$ m in the middle range (52 km) of the data field. With $L = 25$

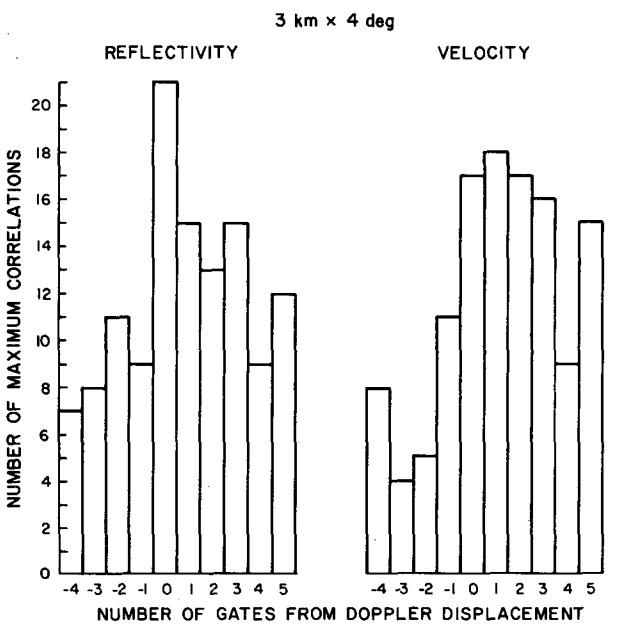

FIG. A1. Histograms showing distribution of maximum correlations about the radial displacement computed from Doppler velocities for 3 km $\times$ 4° boxes.

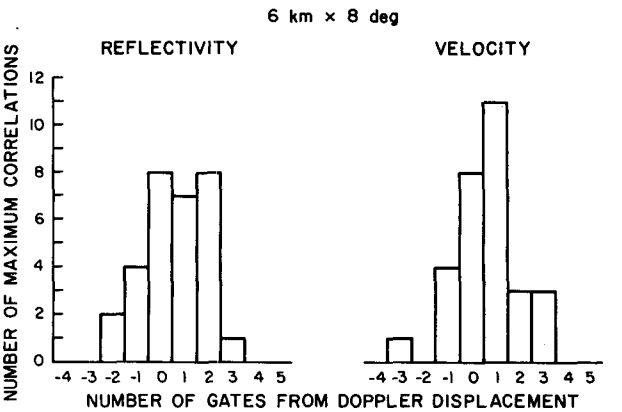

FIG. A2. As in Fig. A1, except 6 km $\times$ 8° boxes.

and $M = 600$ both noise terms in (A9) are more than an order of magnitude less than the signal terms, so that (A9) becomes

$$\text{var}(x) \approx \frac{\sigma(t)\Delta s}{4\sqrt{\pi}} \quad \text{or} \quad \text{S.D.}(x) \approx 220 \text{ m}. \tag{A12}$$

It follows that the standard error in one component of velocity is S.D.(u) $\approx$ S.D.(x/t) $\simeq$ 1 m s^{-1}. Because errors in u and v are independent the magnitude of the total error is $\sqrt{2}$ m s^{-1}. This compares well with the values of 1.6–2.1 m s^{-1} from Fig. 7 at time 210 s.

Our data show evidence that the width of cross-correlation $\sigma(t)$ increases with time lag t. We note (Fig. 7) that the rms error also increases with time and that the curve $\epsilon_T = 0.17\sqrt{\Delta t}$ follows the data very well. If these errors were entirely due to the width of the correlation function [via (A12)] $\sigma(t)$ would be proportional to t^3. But data indicate the increase in width is at most linear with Δt and we must conclude that errors at longer lags are mainly influenced by the anisotropy of the data field.

2. Quantization errors

Errors due to quantization can be computed using

$$\left.\begin{aligned} E_R &= \frac{1}{\sqrt{12}}\frac{\Delta R}{\Delta t} \\ E_\theta &= \frac{1}{\sqrt{12}}\frac{R\Delta\theta}{\Delta t} \end{aligned}\right\}, \tag{A13}$$

where E_R and E_θ, expressed in m s^{-1}, are the velocity errors in range and azimuth, respectively. ΔR is the linear spacing between range gates, Δt the time lag, $\Delta\theta$ the azimuthal increment, and R the distance from the radar to a particular range gate. For our data, $\Delta R = 150$ m, $\Delta\theta = 0.4°$, and a representative $\Delta t = 210$ s. E_R is constant over the entire analysis region

and equals 0.206 m s^{-1} but E_θ varies between 0.259 and 0.672 m s^{-1} at 70 km.

3. Other errors

Another cause of errors is the angular distortion due to widening or narrowing of the second scan correlation regions as the box is shifted in range. We shall look first at the worst possible case of this distortion. The maximum range displacement between correlated boxes in this study was about 90 gates (spaced 1 μs apart) or 13.5 km (for lag Δt = 910 s). Using the relationship $s = R\theta$, where θ is the angular spread of the box in radians, and s is the length of the arc subtended by angle θ, a ratio of the arc length of the box to the arc length of the second correlation region may be found. This is equivalent to the ratio of the ranges, $S_1/S_2 = R_1/R_2$. Say R_1 = 34 km, then R_2 = 20.5 km and we have a distortion S_1/S_2 = 1.66; at most, S_1 would be ⅔ larger than S_2. For a best case situation, we may take a displacement of 16 gates (2.4 km) and R_1 = 67 km. Then R_2 = 64.6 km and S_1/S_2 = 1.04, a distortion of 4%. But actual distortions are only half of these values because the center radials of both the box and the region with which it is correlated are aligned. So, the distortion ranges from about 2 to 33%, which we judge to be tolerable.

Figs. A1 and A2 show the distribution of correlation maxima about the radial displacement predicted by the Doppler velocities within the ±0.75 km spread. For the 6 km × 8° box size (Fig. A2) most correlations maximized within two gates (300 m) of the radial displacement regardless of which quantity was correlated. The distribution for the 3 km × 4° size (Fig. A1) shows a wider spread but still peaks near zero lag from the Doppler indicated radial displacement. These histograms are very representative of other scan pair analyses, and show that, in general, the average Doppler velocity is a good indicator of the radial motion of the air parcel associated with the box.

REFERENCES

Berger, T., and H. H. Groginsky, 1973: Estimation of the spectral moments of pulse trains. Paper presented at the *Int. Conf. Inform. Theory*, Tel-Aviv.

Bjerkaas, C. L., and D. E. Forsyth, 1980: Operational test of a three-dimensional echo tracking program. *Preprints 19th Conf. Radar Meteorology* Miami Beach, Amer. Meteor. Soc., 244–247.

Chandrasekhar, S., 1955: A theory of turbulence. *Proc. Roy. Soc. London,* **A229,** 1–19.

Crane, R. K., 1979: Automatic cell detection and tracking. *IEEE Trans. Geosci. Electron.*, **GE-17,** 250–262.

Doviak, R. J., and M. I. Berger, 1980: Turbulence and waves in the optically clear planetary boundary layer resolved by dual-Doppler radars. *Radio Sci.*, **15,** 297–317.

——, D. S. Zrnic' and D. Sirmans, 1979: Doppler weather radar. *Proc. IEEE*, **67,** 1523–1553.

Hilst, G. R., and J. A. Russo, Jr., 1960: An objective extrapolation technique for semi-conservative fields with an application to radar patterns. Tech. Memo. No. 3, Travelers Weather Research Center, Hartford, CT.

Kessler, E., III, and J. A. Russo, Jr., 1963: Statistical properties of weather echoes. *Preprints 10th Weather Radar Conf.*, Washington, DC, Amer. Meteor. Soc., 25–33.

Kuettner, J., 1959: The band structure of the atmosphere. *Tellus,* **2,** 267–294.

LeMone, M. A., 1973: The structure and dynamics of horizontal roll vortices in the planetary boundary layer. *J. Atmos. Sci.*, **30,** 1077–1091.

Rabin, R. M., R. J. Doviak and A. Sundara-Rajan, 1982: Doppler radar observations of momentum flux in a cloudless convective layer with rolls. *J. Atmos. Sci.*, **39,** 851–863.

Reinking, R. F., R. J. Doviak and R. O. Gilmer, 1981: Clear-air roll vortices and turbulent motions as detected with an airborne gust probe and dual-Doppler radar. *J. Appl. Meteor.*, **20,** 678–685.

Rinehart, R. E., 1979: Internal storm motions from a single non-Doppler weather radar. NCAR/TN-146 + STR, 262 pp.

——, and E. T. Garvey, 1978: Three-dimensional storm motion detection by conventional weather radar. *Nature,* **273,** 287–289.